1   # Orbital CO₂ reconstruction using boron isotopes during the
2   # late Pleistocene, an assessment of accuracy.

3   Elwyn de la Vega[ab], Thomas B. Chalk[ac], Mathis P. Hain[d], Megan R. Wilding[a], Daniel Casey[a], Robin
4   Gledhill[a], Chongguang Luo[ae], Paul A. Wilson[a], Gavin L. Foster[a].

5   [a]School of Ocean and Earth Science, National Oceanography Centre Southampton, University of
6   Southampton, Waterfront campus, Southampton SO14 3ZH, UK.
7   [b]University of Galway, Ollscoil na Gaillimhe, department of Geography, University Road, Galway,
8   H91 TK33, Ireland.
9   [c]Centre Européen de Recherche et d'Enseignement des Géosciences de l'Environnement (CEREGE),
10   Bâtiment Pasteur, Europole Mediterraneen de l'Arbois BP80,13545 Aix-en-Provence cedex 4.
11   [d]Earth and Planetary Sciences, University of California, Santa Cruz, CA, USA.
12   [e]State Key Laboratory of Ore Deposit Geochemistry, Institute of Geochemistry, Chinese Academy of
13   Sciences, Guiyang 550081, P.R. China.

14   Correspondence to Elwyn de la Vega: elwyn.delavega@universityofgalway.ie

15   **Abstract.**

16   Boron isotopes in planktonic foraminifera are a widely used proxy to determine ancient surface seawater
17   pH, and by extension atmospheric CO_2 concentration and climate forcing on geological time scales.
18   Yet, to reconstruct absolute values for pH and CO_2, we require a $\delta^{11}B_{foram-borate}$ to pH calibration and
19   independent determinations of ocean temperature, salinity, a second carbonate parameter, and the boron
20   isotope composition of seawater. Although $\delta^{11}B$-derived records of atmospheric CO_2 have been shown
21   to perform well against ice core-based CO_2 reconstructions, these tests have been performed at only a
22   few locations and with limited temporal resolution. Here we present two highly resolved CO_2 records
23   for the late Pleistocene from ODP Sites 999 and 871. Our $\delta^{11}B$-derived CO_2 record shows a very good
24   agreement with the ice core CO_2 record with an average offset of 4.6 ± 49 (2σ) ppm, and a RMSE of
25   25 ppm, with minor short-lived overestimations of CO_2 (of up to ~50 ppm) occurring during some
26   glacial onsets. We explore potential drivers of this disagreement and conclude that partial dissolution
27   of foraminifera has a minimal effect on the CO_2 offset. We also observe that the general agreement
28   between $\delta^{11}B$ -derived and ice core CO_2 is improved by optimising the $\delta^{11}B_{foram-borate}$ calibration. Despite
29   these minor issues a strong linear relationship between relative change in climate forcing from CO_2
30   (from ice core data) and pH change (from $\delta^{11}B$) exists over the late Pleistocene, confirming that pH
31   change is a robust proxy of climate forcing over relatively short (<1 million year) intervals. Overall,
32   these findings demonstrate that the boron isotope proxy is a reliable indicator of CO_2 beyond the reach
33   of the ice cores and can help improve determinations of climate sensitivity for ancient time intervals.
34

35   ## 1- Introduction.

36   The boron isotope composition of ancient planktonic foraminifera shells is widely used to reconstruct
37   past concentrations of atmospheric CO_2 to understand the drivers and responses of climate change over
38   orbital and geological time scales. Unlike many environmental proxies where it is difficult to assess the
39   accuracy of the resulting reconstructions (e.g. for sea surface temperature), the boron isotope pH/CO_2
40   proxy can directly be compared with the ice core CO_2 records, i.e. the West Antarctic ice sheet divide
41   (Ahn et al., 2012), the EPICA (European Project for Ice Coring in Antarctica) dome Concordia ice core
42   record (Siegenthaler et al., 2005; Luthi et al., 2008; Bereiter et al., 2015), and the Vostock ice core
43   record (Petit et al., 1999). This comparison of CO_2 over the last 800 kyr provides a very powerful test
44   of proxy accuracy. Several past intervals have been studied to test the boron isotope proxy in this way

45 (Sanyal et al., 1995; Foster, 2008; Hönisch and Hemming, 2005; Henehan et al., 2013; Raitszch et al.,
46 2018).

47 Given the success of these comparisons, the boron isotope proxy has been used to investigate the
48 interaction between CO2, the ocean carbon cycle and climate beyond the reach of the ice cores, such as
49 during the Mid-Pleistocene transition (Hönisch et al., 2009; Chalk et al., 2017; Dyez et al., 2018), the
50 Pliocene (Martinez-Boti et al., 2015, de la Vega et al., 2020), the Miocene (Foster et al., 2012; Greenop
51 et al., 2014, Guillermic et al., 2022), the Eocene (Anagnostou et al., 2016, 2020; Harper et al., 2020),
52 Paleocene-Eocene boundary (Penman et al., 2014; Gutjahr et al. 2017) and the Cretaceous-Palaeogene
53 boundary (Henehan et al., 2019). Application of the boron isotope proxy is however complicated by the
54 need for: (i) an empirical species-specific calibration of $\delta^{11}B_{foraminifera}$ to $\delta^{11}B_{borate}$ in the pH expression
55 (Henehan et al., 2013, 2016, hereafter $\delta^{11}B_{foram-borate}$ calibration), sometimes including extinct species
56 for deep-time reconstruction; (ii) $\delta^{11}B$ of seawater ($\delta^{11}B_{sw}$), temperature and salinity in the past to
57 calculate pH from $\delta^{11}B$; and (iii) a second carbonate parameter (typically total alkalinity, total dissolved
58 inorganic carbon, DIC, or calcite saturation state) to convert pH to CO2. While these variables do not
59 influence the magnitude of uncertainty equally in all time intervals, assessment of the boron-based
60 reconstructions against existing ice-core records is a powerful test of the proxy's accuracy.
61
62 Recently, Hain et al. (2018) suggested that the radiative forcing from CO2 change (ΔF_{CO2}) is linearly
63 related to pH change (ΔpH) of equilibrated water of the low-latitude surface ocean when the CO2 change
64 occurs faster than the residence time of carbon with respect to silicate weathering (e.g., ~1 million years
65 (Myr)). That is, glacial/interglacial CO2 climate forcing could be estimated directly from reconstructed
66 ΔpH. Given that one of the main priorities for accurate reconstructions of past CO2 levels is to allow
67 determinations of climate sensitivity, defined as the temperature response to a radiative forcing –
68 typically a doubling of CO2 with associated slow and fast feedbacks (e.g. Rohling et al., 2013, 2018) –
69 this recognition may provide a useful shortcut. Climate forcing is a perturbation of the planet's energy
70 balance averaged over the planet (Hansen et al., 2008) and CO2 forcing, ΔF_{CO2} expressed in W.m^{-2}, at a
71 given time can be written as:

72 $$\Delta F_{CO2} \cong \alpha_{2xCO2} * \frac{\Delta \log_{10} CO_2}{\log_{10} 2} \ (1)$$

73 where α_{2xCO2} is the sensitivity of the radiative balance per doubling of CO2, and $\Delta \log_{10}CO_2$ is the CO2
74 change over time expressed in terms of how many 10-foldings of proportional (not absolute) CO2
75 change (Hain et al., 2018).
76
77 By considering basic equilibrium reactions of carbon species, $\Delta \log_{10}CO_2$ can be derived and expressed
78 as:
79
80 $$\Delta \log_{10} CO_2 \cong \Delta \log_{10} DIC + \Delta pK_0 + \Delta pK_1 - \Delta pH \ (2)$$
81
82 Hain et al. (2018) showed that the terms $\Delta \log_{10}DIC$ and $\Delta pK_0 + \Delta pK_1$ are small and that $\Delta logCO_2$ can
83 therefore simply be expressed as :
84
85 $$\Delta \log_{10} CO_2 \cong -\Delta pH \ (3a)$$
86
87 $$\Delta F_{CO2} \cong -\frac{\log_{10} 2}{\alpha_{2xCO2}} \Delta pH \ \cong -12.3 \Delta pH \ (3b)$$
88
89 To assess the uncertainty of this approximate -1:1 $\Delta \log_{10}CO_2/\Delta pH$ relationship Hain et al. (2018)
90 considered three different end-member causes to compute the accurate $\Delta \log_{10}CO_2/\Delta pH$ relationship: (1)
91 DIC addition/removal yields a slope of -1.3:1 (relative to the basic formalism), (2) CaCO3
92 addition/removal (e.g. precipitation/dissolution, riverine input) yields a slope of -0.9:1, and (3)
93 warming/cooling yields a slope of -1.1:1. That is, even if ΔpH was known exactly this range of plausible
94 slopes results in estimated $\Delta \log_{10}CO_2$ and ΔF_{CO2} that are systematically biased by -10% for change
95 caused purely by CaCO3 variations or +30% for change purely caused by DIC variations relative to the

96 approximate -1:1 $\Delta\log_{10}CO_2/\Delta pH$ relationship. While introducing such structural uncertainty in the
97 estimation of ΔF_{CO2} is a concern, this approach eliminates the need to assume a second carbonate system
98 parameter and the uncertainty incurred thereby. An estimate of $\delta^{11}B_{sw}$ is still needed to reconstruct pH
99 based on the boron isotope proxy system (Foster and Rae, 2016) but estimated pH change (i.e., ΔpH) is
100 much less sensitive to error in assumed $\delta^{11}B_{sw}$ than is absolute pH (Hain et al., 2018). An important
101 caveat to estimating ΔF_{CO2} directly from ΔpH is that the intercept of the $\Delta\log_{10}CO_2/\Delta pH$ relationship
102 can change with silicate weathering carbon cycle dynamics thought to be important on a million year
103 timescale, such that the approach is applicable for orbital timescale variability and short-term shifts but
104 not for long-term trends in ΔF_{CO2}. Therefore, the orbital timescale ice age cycles of atmospheric CO_2
105 reconstructed from air occluded in Antarctic ice cores offer a unique opportunity to determine the
106 $\Delta\log_{10}CO_2/\Delta pH$ relationship observationally and compare to theory. Furthermore, Hain et al., (2018)
107 raise the possibility that the $\Delta\log_{10}CO_2/\Delta pH$ relationship could be decomposed based on the different
108 end-member slopes to constrain the relative importance of the mechanism causing the pH and CO_2
109 changes.

110

111 In light of these recent advances, our aims here are twofold. First, we extend previous ice-core validation
112 studies (Foster, 2008; Henehan et al. 2013; Chalk et al., 2017) and test the extent to which boron
113 isotopes reconstruct CO_2 faithfully when current methods and assumptions are applied. In contrast to
114 most previous studies, we use two deep ocean sites and present $\delta^{11}B$ and CO_2 data at high temporal
115 resolution (1 sample every ~3 to 6 kyr). This enables: (i) a thorough test of the assumptions typically
116 made including the central tenet of atmospheric CO_2 proxies that surface ocean CO_2 remains in
117 equilibrium with the atmosphere over time at any given site, (ii) an evaluation of the overall uncertainty
118 of the proxy; (iii) an evaluation of the influence of variable foraminiferal preservation on the accuracy
119 of the CO_2 reconstructed; and (iv) a refinement of a number of the input assumptions and uncertainties,
120 including the $\delta^{11}B_{borate\text{-}foram}$ calibration. Second, we evaluate the approach of Hain et al. (2018) and
121 assess the robustness of pH change to not only provide insights into the magnitude of climate forcing
122 from CO_2 change, but also the ability of this approach to provide insights into the causes of CO_2 change
123 over glacial-interglacial cycles.

124 **2.   Methods.**

125 **2.1   Core location and oceanographic setting.**

126 To accurately reconstruct atmospheric CO_2 with the $\delta^{11}B$-CO_2 proxy, it is essential to measure $\delta^{11}B$ in
127 foraminifera from locations where the CO_2 flux between the ocean and the atmosphere is in near
128 equilibrium. We therefore target regions of the ocean where the water column is stratified and
129 oligotrophic as these regions are most likely to attain this condition (Takahashi et al., 2009). Here,
130 following previous studies (Foster, 2008, Henehan et al., 2013; Chalk et al., 2017), we report data from
131 ODP Site 999 (Figure 1, 12.75°N, 78.73°W, water depth 2827 m, sedimentation rate 3.7 cm/ky) in the
132 Caribbean and supplement this well studied site with samples from ODP Site 871 in the Western Pacific
133 (5.55°N, 172.35°E, water depth 1255m, sedimentation rate ~1 cm/ky). The sediments studied at ODP
134 Site 871 are shallowly buried and the site today features a deep thermocline and is located off the
135 equator, hence they are unlikely to be influenced by significant equatorial upwelling (Dyez and Ravelo,
136 2013, 2014). These two sites show a minor annual mean disequilibrium of +12 ppm (range ~0 to ~30
137 ppm, Takahashi et al., 2009) for ODP Site 871, and +21 ppm (Olsen et al., 2004; Foster, 2008) for ODP
138 Site 999. These disequilibria are used to correct our CO_2 data derived from $\delta^{11}B$ and are assumed to be
139 constant throughout the entire record presented here.

140

141
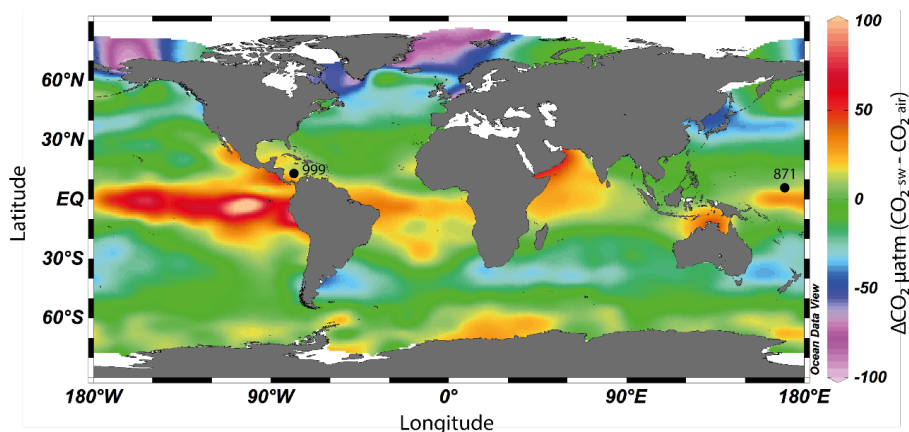
142
143 Figure 1. Map of air-sea CO_2 disequilibrium (seawater – air) in ppm and location of ODP sites used in this study.
144 CO_2 data from Takahashi et al. (2009). The map was made with Ocean Data View (Schlitzer, 2022).

145 **2.2 Samples.**

146 *2.2.1 Sample selection and preparation.*

147 Samples of deep-sea sediment from our two study sites were taken at 6cm (~3ky) and 10cm (~6ky)
148 resolution at ODP 871 and 999 respectively. Around 1-2 mg of the foraminifer (between 120 and 200
149 individuals) from the species *Globigerinoides ruber sensu stricto white* (here after *G. ruber ss*) were
150 hand-picked from the size fraction 300-355 4µm for a target of 10 to 20 ng of boron. *G. ruber ss* was
151 chosen here because it is readily identified, is abundant throughout our chosen time interval and a
152 $\delta^{11}B_{foram-borate}$ calibration that accounts for vital effects is available from culture, plankton tows and core-
153 top samples (Henehan et al., 2013). It is also known to live in the upper surface of the ocean with a
154 relatively small depth range which prevents significant influence of deeper more remineralised CO_2-
155 rich waters on the measured $\delta^{11}B$. The morphotype *G. ruber sensu lato* (hereafter *G. ruber sl*) has
156 slightly different morphology (Aurahs et al, 2001; Carter et al., 2017) and is thought to live in deeper
157 water compared to *G. ruber ss* (Wang, 2000). The morphotype *G. ruber sl* was also hand separated and
158 analysed at lower resolution at ODP 871 to monitor any change over time in morphotype differences in
159 $\delta^{11}B$ that could result from different habitats. For similar reasons, carbon and oxygen isotopes ($\delta^{18}O$
160 and $\delta^{13}C$) were also measured on *G. ruber ss* and *sl* for comparison on the whole record at ODP 871.
161 For this, around 10 individuals of *G. ruber* per sample were picked, their shells gently broken open and
162 mixed and then a 100 µg aliquot of the homogenised carbonate was measured using a Thermo KIEL IV
163 Carbonate device at the University of Southampton, Waterfront Campus.
164

165 *2.2.2 Age constraints.*

166 Samples were taken from 1.5 to 5 metres below sea floor (mbsf) for ODP 871 and from 9 to 21 mbsf
167 for ODP 999. Sample age at Site 871 was initially determined from sample depth using published age
168 models (Dyez and Ravelo, 2013). At Site 999, the age was determined by developing a new benthic
169 $\delta^{18}O$ record. The initial age model at Site 871 was refined by measuring $\delta^{18}O$ on the benthic species
170 *Cibicoides wuellerstorfi* (50 µg of 3-5 mixed, crushed and homogenised specimens) measured on a
171 Thermo KIEL IV Carbonate device at the University of Southampton, Waterfront Campus. These new
172 $\delta^{18}O$ data (Figure 2) were then tuned to the benthic $\delta^{18}O$ LR04 stack (Lisiecki and Raymo, 2005) using
173 Analyseries (Paillard et al., 1996).
174

175   *2.2.3   Fragment counts.*

176   Foraminifera fragment counts were conducted on ODP Site 871 to monitor variations in carbonate
177   preservation. Samples were sub-sampled using a splitter (in order to maintain homogeneity) and poured
178   onto a picking tray. The fragmentation index (FI) was calculated following the approach of Howard and
179   Prell (1994) and Berger (1970) where percentage fragment is defined as:
180

181
$$FI = 100 * \frac{\text{number of fragments}}{\text{number of fragments} + \text{number of whole tests}} \quad (4)$$

182

183   Counts of whole intact grains and fragments of grains were conducted three times and averaged. The
184   standard deviation (1σ) of the fragmentation index is 1.69. This approach followed that used in an early
185   study at ODP Site 999 (Schmidt et al. 2006) ensuring that the datasets between the two sites are
186   comparable

187   *2.2.4   Boron separation.*

188   The hand separated foraminifera tests for boron isotope analysis were broken open, detrital clay was
189   removed, and oxidatively cleaned and leached in a weak-acid to obtain a primary carbonate signal using
190   established methods (Barker et al., 2003). Samples were then slowly dissolved in ~ 100 μl 0.5M HNO_3
191   added to 200 μl of MQ water. Dissolved samples were then centrifuged for 5 minutes to separate any
192   remaining undissolved contaminants (e.g. silicate grains, pyrite crystals) and transferred to screw top 5
193   ml Teflon pots for subsequent boron separation. An aliquot equivalent to 7% of each sample was kept
194   for elemental analysis and transferred to acid cleaned plastic vials in 130 μl 0.5M HNO_3. Samples were
195   purified for boron using anion exchange column chemistry method prior to isotope analysis as described
196   elsewhere (Foster, 2008). A total procedure blank (TPB) was conducted for each batch of samples and
197   typically ranged from 0-50 pg which represents a very small contribution relative to our sample size (0-
198   0.25%), hence no samples required correction in this study.

199   **2.3   Effect of dissolution (leaching experiment).**

200   To investigate the effect of partial dissolution on measured $\delta^{11}B$, a leaching experiment was conducted
201   on two species of commonly analysed planktic foraminifera: *G. ruber ss* and *Trilobatus sacculifer*
202   (hereafter *T. sacculifer*). Around ~ 180 *G. ruber ss* (size 300-355 μm) and 40 *T. sacculifer* (size 500-
203   600 μm) were picked four times and the samples were treated like so: one split was the control and
204   received no treatment, and the three other samples (whole foraminifera) were placed in 0.0001 M Teflon
205   distilled HNO_3 (pH 4) for 2, 4, and 6 hours respectively. The experiment was repeated for *G. ruber ss*
206   by longer treatments, up to 10 hours in the dilute acid. The foraminifera subjected to these partial
207   dissolution tests were then treated using the same cleaning and chromatography protocols described
208   above.
209

210   We acknowledge that our leaching tests aren't as thorough as those described in some other studies
211   (e.g. Brown and Elderfield, 1996; Sadekov et al., 2010) but provide useful first-order insights into the
212   susceptibility of $\delta^{11}B$ to partial dissolution of foraminiferal tests.

213   **2.4   Analytical techniques**

214   Boron isotope analyses were performed on a ThermoScientific Neptune multi collector inductively
215   coupled plasma mass spectrometer (MC-ICPMS) with 10^{12} W amplifier resistors using a standard-
216   sample bracketing routine with NIST 951 boric acid standard (following Foster et al. 2013 and Foster,
217   2008). Elemental analysis was performed on each dissolved sample using a ThermoScientific Element
218   inductively coupled plasma mass spectrometer (ICPMS). All analyses were carried out at the University
219   of Southampton, Waterfront Campus (following Foster, 2008 and Henehan et al., 2015). Element to
220   calcium ratios were measured with ^{43}Ca and ^{48}Ca and measured against in house mixed element

221 standards. Elemental ratios measured included: B/Ca, Mg/Ca, Al/Ca, Mn/Ca, Sr/Ca. Based on the
222 reproducibility of our in-house standards, the uncertainty for most elemental ratios is ~ 5% (at 95%
223 confidence).

224 **2.5 Constraints on δ^{11}B-derived pH and CO$_2$.**

225 *2.5.1   From δ^{11}B to pH.*

226 Seawater pH is related to the boron isotopic composition of dissolved borate ion by the following
227 equation:
228

229
$$pH = pK_B - \log\left(-\frac{\delta^{11}B_{sw} - \delta^{11}B_{borate}}{\delta^{11}B_{sw} - a_B * \delta^{11}B_{borate}(a_B - 1)}\right) \quad (5)$$

230

231 where the isotopic fractionation factor α_B between $B(OH)_3$ and $B(OH)_4^-$, is 1.0272 as determined by
232 Klochko et al. (2006) and the δ^{11}B of seawater is 39.61 ‰ (Foster et al., 2010) for both sites and kept
233 constant throughout the record due to the long residence time of boron (10-20 Myrs, Lemarchand et al.
234 2002).

235

236 The sea surface temperature (SST) values necessary to calculate pK_B in equation (5) were determined
237 at both sites using the Mg/Ca of *G. ruber* and the relationship of Anand et al. (2003):
238

239
$$SST = \frac{\ln\left(\frac{\frac{Mg}{Ca}_{surf}}{0.38(\pm0.02)}\right)}{0.09(\pm0.003)} \quad (6)$$

240

241 This calibration does not include a depth correction but yields temperatures from core top samples that
242 are consistent with modern SST (Olsen et al., 2016). The salinity that is used in the expression of pK_B
243 is kept constant for both sites (35 PSU) due to the very minor effect of salinity on calculated CO$_2$.

244

245 To investigate the effect of the recently proposed pH effect on reconstructed Mg/Ca-derived SST and
246 hence reconstructed CO$_2$, we've explored a scenario wherein we apply a pH correction on Mg/Ca-SST
247 using the iterative approach of Gray and Evans (2019).

248 *2.5.2   From pH to CO$_2$.*

249 Calculating CO$_2$ from boron isotope derived pH is dependent on the determination of a second
250 parameter of the carbonate system. Here we use the modern value of total alkalinity (TA) at each site:
251 2279 and 2350 µmol/kg at ODP 871 and ODP 999, respectively (Shipboard Scientific Party, 1993;
252 Takahashi et al., 2009). Following Chalk et al. (2017), these values were kept constant throughout the
253 whole record. To account for any variations in alkalinity, a generous uniform (or flat) uncertainty of
254 175 µmol/kg is applied (i.e. equal likelihood of values within the range of uncertainty). This range in
255 TA encompasses the likely range in this variable on glacial-interglacial (e.g. Toggweiler, 1999; Hain et
256 al., 2010; Cartapanis et al., 2018) or longer timescales (Hönisch et al. 2009), and its adoption means the
257 local site is not tied to a global sea-level record as had been practice previously. We avoid drawing this
258 link because the ~+3% (+68µmol/kg) concentration increase of solute alkalinity occurring from sea-
259 level lowering during the last glacial maximum may not have been the dominant driver of ocean
260 alkalinity change (Boyle, 1988a/b; Sigman et al., 1998; Toggweiler, 1999; Hain et al., 2010; Cartapanis
261 et al., 2018). By assuming a uniform distribution for TA we avoid imposing a temporal evolution to this
262 variable because evolution of TA through a glacial cycle is uncertain and is unlikely to be simply a
263 function of sea-level or salinity (e.g. Dyez et al. 2018) due to the effect of carbonate compensation.

264 The surface water CO$_2$ is then calculated as (Zeebe and Wolf-Gladrow, 2001):
265
266

267
$$CO_2 = \frac{TA - \frac{K_B * B_T}{K_B + [H^+]} - \frac{K_W}{[H^+]} + [H^+]}{\frac{K_1}{[H^+]} + \frac{2 K_1 K_2}{[H^+]^2}} \quad (7)$$

268

269 where TA is the total alkalinity, K_B the equilibrium constant of boron species in seawater, B_T the
270 concentration of boron in seawater (432.6 μmol/kg, Lee et al., 2010), [H$^+$] the concentration of H$^+$
271 determined from pH = - log [H$^+$], K_W the dissociation constant of water (function of T, S and pressure),
272 K_1 and K_2 the first and second dissociation constants of carbonic acid (function of T, S and pressure,
273 Luecker et al., 2000). The estimate of atmospheric CO_2 includes site-specific offsets relative to
274 reconstructed surface water CO_2 to account for observed local disequilibrium (+21 ppm and +12 ppm
275 at ODP Sites 999 and 871, respectively).

276 **2.6 Uncertainty.**

277 *2.6.1   Analytical uncertainty.*

278 The uncertainty on the measured $\delta^{11}B$ is expressed as the external uncertainty which includes
279 instrumental error and chemical separation of the sample (see a detailed discussion in John and Adkins,
280 2010). This was determined empirically by long-term repeat measurements of JCp-1 subject to the same
281 chemical purification as our foraminiferal samples. As discussed by Rae et al. (2011) this uncertainty
282 is dependent on the intensity of the ^{11}B signal and is expressed here by the following relationship defined
283 during the duration of this study at the University of Southampton (Anagnostou et al., 2019), for ^{11}B
284 intensities <0.54V:

285
$$2\sigma = 129600 \ e^{-212 \ x \ [^{11}B]} + 0.3385 \ e^{-1.544 \ x \ [^{11}B]} \quad (8).$$

286

287 where [^{11}B] is the intensity of ^{11}B signal in volts. The $\delta^{11}B$ uncertainty for ^{11}B intensities > 0.54V is
288 0.15‰ (at 95% confidence).

289 *2.6.2   pH and CO_2 uncertainty.*

290 The CO_2 uncertainty we report was calculated with a Monte Carlo simulation (10, 000 realisations) in
291 order to fully account for the uncertainty in all variables used in the calculation of pH and CO_2 (σ_{CO2}
292 $_{\delta11B-derived}$). The shape of the uncertainty distribution sampled is either normally distributed (for
293 temperature, salinity and $\delta^{11}B$) or uniform (for alkalinity, as discussed above). The maximum
294 probability of all realisations was used as the central value for CO_2 and an error envelope at 1 and 2σ
295 was calculated based on the 68% and 95-% distribution of the realisations.

296

297 *2.6.3   Uncertainty on the CO_2 offset*

298 To constrain the offset between $\delta^{11}B$-derived CO_2 and ice core CO_2, each sediment age is compared to
299 the ice core CO_2 record by interpolation of the record of highest resolution (in this case the $\delta^{11}B$ record
300 onto the ice core compilation). To fully account for age uncertainty when interpolating the sediment
301 age to the well-dated ice core record, a distribution of the ice core data was calculated within the 4σ
302 uncertainty of the $\delta^{11}B$ age and weighed by the respective likelihood based on the age difference
303 between ice core and sediment core.

304

305 The CO_2 offset (or residual) is defined by:

306

307
$$Offset_{CO2} = CO_2 \ _{\delta11B-derived} - CO_2 \ _{ice} \quad (9)$$

308

Climate
of the Past

Discussions

309 The uncertainty on this offset (σ_{offset}) accounts for the uncertainty of the interpolated ice core CO_2
310 ($\sigma_{\text{CO2.interpol}}$) and the one of the $\delta^{11}B$-derived CO_2 ($\sigma_{\text{CO2.}\delta11B\text{-derived}}$), such as :
311
312

313 $$\sigma_{\text{offset}} = \sqrt{\sigma^2_{\text{CO2.interpol}} + \sigma^2_{\text{CO2.}\delta11B-\text{derived}}} \quad (10)$$

314 **2.7 The relationship between $\delta^{11}B$ -derived pH and ΔF_{CO2}.**

315 The linear relationships between the relative CO_2 forcing ΔF_{CO2} and pH are determined with a York
316 regression (York et al., 2004) that accounts for the uncertainty in both the independent and dependent
317 variable (i.e. x and y axes). The ice core CO_2 interpolation used to calculate ΔF_{CO2} and uncertainty is
318 determined as described in section 2.6 (Hain et al., 2018).

319 **2.8 Optimising the *G. ruber* $\delta^{11}B$ borate-foraminifera calibration.**

320 An optimised *G. ruber* calibration was obtained by minimising the root mean square error (RMSE) of
321 the average offset between $\delta^{11}B$-derived CO_2 and ice core CO_2. The steps are illustrated in Figure S1.
322 In order to optimise the calibration, 10,000 simulations of $\delta^{11}B_{\text{borate}}$ and $\delta^{11}B_{\text{foraminifera}}$ from the calibration
323 of Henehan et al. (2013) were performed within their normally distributed uncertainty (1σ), from which
324 we defined the same number of linear models each including their slope and intercept. Then, we
325 calculate the equilibrium pH and resultant equilibrium $\delta^{11}B_{\text{borate}}$ from ice core CO_2 and the assumed
326 constant TA at each core site. The $\delta^{11}B_{\text{borate}}$ from the 10,000 linear models is then calculated and the
327 difference to the ice core-derived $\delta^{11}B_{\text{borate}}$ is determined. The linear model calibration that yields the
328 minimum RMSE between these two borate variables defines the new $\delta^{11}B_{\text{borate-foram}}$ calibration. Unless
329 indicated otherwise, the pH results presented in this study are calculated with the published calibration
330 (Henehan et al., 2013), and the results with the optimised calibration presented in section 4.2.6.

331 **3   Results.**

332 **3.1 Temperature and fragment counts.**

333 The SST at ODP Sites 999 and 871 show a cyclicity that agrees with the well-known glacial interglacial
334 cycles of the late Pleistocene (Figure 2). The Mg/Ca-SST corrected for pH (Figure S2) shows lower
335 temperatures of about 0.2 to 2.5°C, yet the glacial variation structure is maintained. The SST determined
336 from *G. ruber sl* Mg/Ca uncorrected (red filled circles, Figure 2B) at Site 871, show systematically
337 cooler temperatures than *G. ruber ss* (black filled circles). The fragmentation index (Figure 2) at ODP
338 871 range from 20 to 50 % and follow the well-documented "Pacific style" dissolution cycles (Sexton
339 and Barker, 2012) with well-preserved carbonate (low fragments) during glacials and less well-
340 preserved carbonates (higher fragments) during interglacials. The percentage sand typically
341 anticorrelates with fragmentation counts at both sites, although it is less clear at ODP 999, perhaps due
342 to the shorter record available. Fragmentation counts reach maxima at ODP 999 of 20 % during
343 interglacials and up to 50 % during marine isotope stage MIS 11 which is concomitant with the mid-
344 Brunhes dissolution interval (MBDI, Barker et al., 2006). The fragmentation counts at ODP 871 show
345 no substantive anomaly during the MBDI.
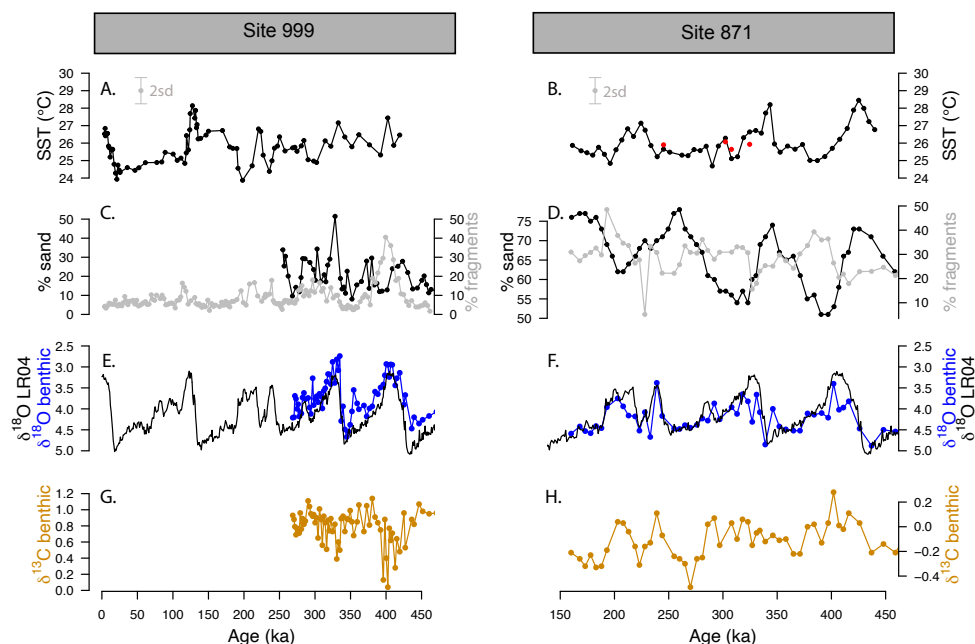
Figure 2. Mg/Ca derived temperature, coarse fraction (sand), fragmentation and benthic $\delta^{18}O$ and $\delta^{13}C$ at ODP sites 999 and 871. **A, B:** Temperature at ODP 999 (from *G. ruber ss*, black, Schmidt et al., 2006) and ODP 871 (*G. ruber ss*, black, *G.ruber sl*, red, 2sd indicated by the grey error bar). **C, D:** Fragmentation index (light grey, data from Schmidt et al. (2006) for ODP 999) and sand (black line). **E, F:** Benthic *C. wuellestorfi* $\delta^{18}O$ (blue) and LR04 benthic $\delta^{18}O$ stack (black). A correction of +0.48‰ is applied to our $\delta^{18}O$ data in order to adjust for species offset between *C. wuellestorfi* and LR04. **G, H:** Benthic *C. wuellestorfi* $\delta^{13}C$ (orange).

3.2 pH and CO₂ reconstructions.

The $\delta^{11}B$, pH and $\delta^{11}B$-derived absolute CO_2 (Figure 3) from Sites 871 and 999, show clear cyclicity related to glacial-interglacial cycles. The CO_2 values carry an average uncertainty of ±48 ppm and the mean offset from the ice core CO_2 for a combination of the two records is 4.6 ±49 (2σ) ppm showing that there is a minor overestimation of CO_2 using the boron method yet it agrees on average well within uncertainty. The RMSE of the CO_2 offset for the combined record is 25 ppm.

Despite the overall close agreement between $\delta^{11}B$-derived CO_2 and ice core-derived CO_2, each of our $\delta^{11}B$-CO_2 records exhibit some short-lived intervals where the offsets from the ice core record are larger. This is further revealed by the residual CO_2 and the identification of the data above the upper quartile (i.e. the upper 25% of the data, Figure S3). Those data do not appear to be randomly distributed and instead occur at ~100 ky, ~220-290 ky and ~390 ky at ODP Site 999, in all three cases during the early stages of the glaciation (except for the MIS 8 glacial at 280ky, Figure S3). The mismatches with the ice core at ODP Site 871 show a similar temporal pattern occurring at ~220 and ~300 and ~ 390 ky (i.e. at glacial inceptions).

Climate
of the Past
Discussions

369
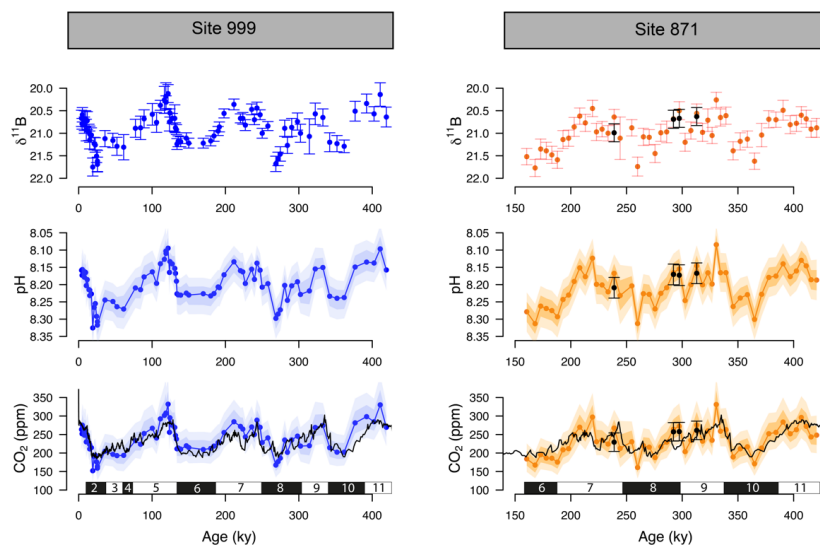
Figure 3. $\delta^{11}B$, pH and boron-derived CO_2 at site 999 and 871. $\delta^{11}B$ of *G. ruber ss* and *sl* (top row), boron-derived pH (middle row) and CO_2 (bottom row) reconstruction from two core locations: ODP 999 (blue, this study and published data, Foster, 2008; Henehan et al., 2013; Chalk et al., 2017) and ODP 871 (orange, this study). The black line in the CO_2 panels is the composite Antarctic ice core CO_2 record (Bereiter et al., 2015). All $\delta^{11}B$-derived data points are from *G. ruber ss* except black dots at ODP Site 871 measured on *G. ruber sl*. Numbers at the bottom of the CO_2 records represent marine isotope stages (Black box for glacials and white box for interglacials). Note the age scale is different at site 999 and 871.

3.3 Contrasting $\delta^{11}B$ between morphotypes.

Within error, the few measurements of $\delta^{11}B$ *G. ruber sl* at ODP 871 all agree with $\delta^{11}B$ *G. ruber ss* (Figure 3) albeit the $\delta^{11}B$ of *G. ruber sl* is higher than *G. ruber ss* for all 4 data pairs available. The CO_2 derived from *G. ruber sl* (Figure 3) is on average 15 ppm lower than the one derived from *G. ruber ss*; though the much lower resolution (n=4) impedes a thorough comparison at this stage. The $\delta^{18}O$ and $\delta^{13}C$ of both morphotypes were compared for the whole records at ODP 871 (Figure S4) and a cross-plot shows a moderate to good agreement between *G. ruber ss* and *sl* (r^2=0.55 and 0.22 for $\delta^{18}O$ and $\delta^{13}C$ respectively, Figure S5). This is in contrast to other studies (e.g. Wang et al., 2000; Steinke et al., 2005) that show $\delta^{18}O$ in *G. ruber sl* to be systematically higher.

3.4 Dissolution experiments.

The leaching experiments on *T. sacculifer* and *G. ruber ss* show a different response for the two species (Figure S6). While *G. ruber ss* show no significant variation in measured $\delta^{11}B$ under different treatments, *T. sacculifer* shows no systematic variations in $\delta^{11}B$ for the control and first two treatments (leached in 2 and 4 hours in 0.0001M HNO_3, pH 4) but shows a ~1‰ shift (relative to the control) towards lighter $\delta^{11}B$ after 6 hours at pH 4.

3.5 Relationship between δ^{11}B-pH and CO_2 forcing from the ice core.

A cross plot of δ^{11}B-derived pH CO_2 forcing from the ice core record for each of our marine core study sites is shown in Figure 4 and is compared to the theoretically-derived approximate $\Delta FCO_2/\Delta pH$ relationships as adopted by Hain et al. (2018): -1:1 W/m^2 (dashed black line); $CaCO_3$ addition/removal (-0.9:1 W/m^2 plain yellow line); DIC addition/removal (-1.3:1 W/m^2 dotted-dashed blue); and warming/cooling temperature forcing (-1.1:1 W/m^2, dashed red). Our analysis includes full propagation of uncertainty in pH, in contrast to Hain et al. (2018) who considered only the reported uncertainty of $\delta^{11}B_{borate}$ in their validation exercise. In both cases the uncertainty in ΔF_{CO2} accounts for the error in interpolation arising when comparing age-uncertain δ^{11}B-derived pH with ΔF_{CO2} from the well-dated and high-resolution ice core CO_2 record (see methods 2.7 and 2.6 for details). This treatment of ΔF_{CO2} uncertainty is dominated by the spread of ice core CO_2 data points within the δ^{11}B age uncertainty. The data are fitted with a York-type regression (thin black line; York et al., 2004) where the grey envelope represents the uncertainty of the linear relationship that best represents the data (i.e., the envelope is not the prediction interval), considering the uncertainty in pH and ΔF_{CO2}. The regressed slope is $\Delta F/\Delta pH = -15.42 \pm 0.8$ W/m^2 (-1.2:1 relative to basic formalism) and shows a good agreement with the theoretical temperature and DIC driven relationships.

The effect of the uncertainty assigned to pH (fully propagated or using the measurement uncertainty of the boron isotope) on the regressed slope is shown in Figure S7. The slope of the York regression when using the uncertainty from δ^{11}B only, as in Hain et al. (2018), shows a very close agreement with the basic formalism, with a slope of $\Delta F/\Delta pH = -12.4 \pm 0.3$ W/m^2, (-1:1 relative to the basic formalism) but with a unsatisfactory goodness of fit (mean square weighted deviation, mswd) of 6, whereas propagating the full pH uncertainty based on our iterative Monte-Carlo simulations improves goodness of fit to ~1 at a $\Delta log_{10}CO_2/\Delta pH$ of -1.2:1 (Figure 4).
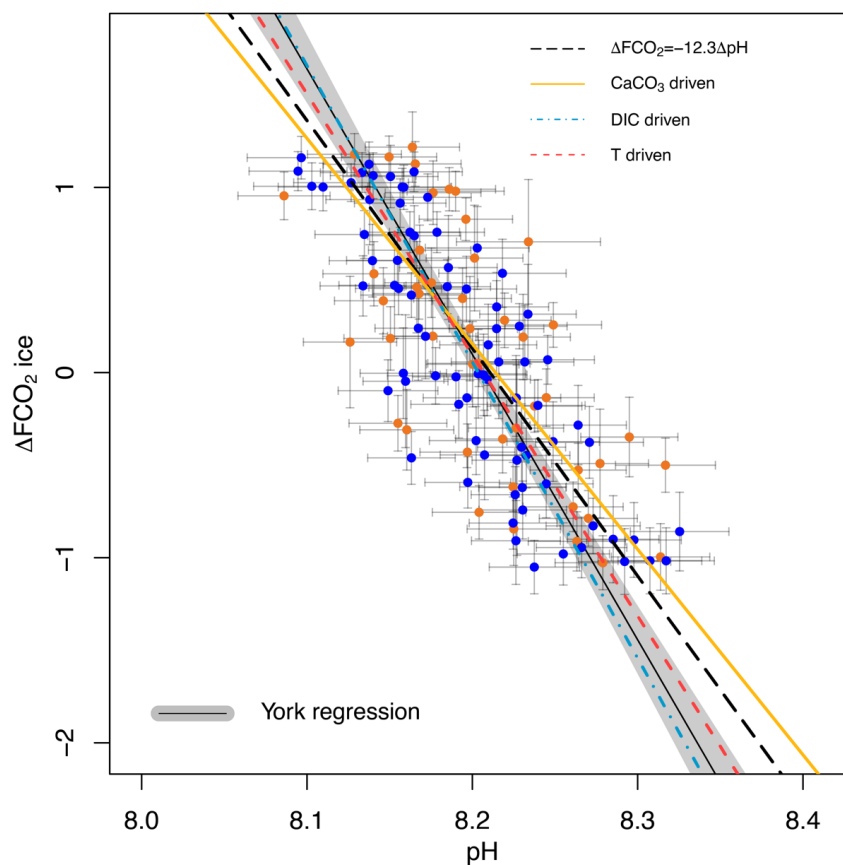
Figure 4. Ice core based ΔFCO_2 (CO_2 forcing) vs. $\delta^{11}B$-based pH for ODP 999 (blue filled circles, this study and published data from Foster, 2008; Henehan et al., 2013; Chalk et al., 2017) and 871 (orange filled circles). The lines show the relationship between ΔFCO_2 and pH for the simplified formalism (see method) $\Delta FCO_2 = -12.3\Delta pH$ (black dashed line), and when driven by changes in DIC only (blue, $\Delta F/\Delta pH = -16$ W/m^2), CaCO$_3$ (yellow, $\Delta F/\Delta pH = -11.1$ W/m^2) and temperature T (red, $\Delta F/\Delta pH = -14.1$ W/m^2). The York regressed line (black line and grey shade) falls between the theoretical only pH-driven line (black) and CaCO$_3$ line (yellow).

4   Discussion.

4.1 Cyclicity in foraminifera preservation.

Percentage fragments and sand fraction ($> 63\mu$m) at both studied core sites are anticorrelated and show a clear cyclicity, with better preservation of carbonates during glacial periods (Figure 2). The anticorrelation is clearer at ODP 871 where we have the longest record (Figure 2). Sexton and Barker (2012) suggest that this Pacific Ocean pattern of preservation (Farrell and Prell, 1989) initiated after the mid Pleistocene transition (MPT) around 1 Ma, and that preservation cycles in the Pacific prior to MPT showed a more "Atlantic style" of dissolution with better (poorer) preservation occurring during interglacials (glacials). Several data sets (deep oxygen and carbon isotopes, carbonate ion data, and sortable silt) point towards a strengthening of ventilated deep Pacific waters (lower circumpolar deep water LCDW) that lead to the better preservation during glacials in the Pacific after the MPT (Sexton and Barker, 2012).

436   The observation that the fragmentation records of sites 999 and 871 covary is likely attributable to the
437   different water masses that fill the Caribbean basin relative to the rest of the Atlantic basin. During
438   glacials, the deep Atlantic is filled by nutrient- and carbon-rich corrosive southern sourced waters
439   (Antarctic Bottom Water, AABW) with a reduced contribution from the less corrosive, nutrient-poor
440   North Atlantic Deep Water (NADW) (Oppo and Lehman, 1993) causing calcareous sediments in the
441   deep Atlantic Ocean >2500 m to be less well-preserved during glacials than interglacials. The opposite
442   pattern of dissolution is seen in the Caribbean because shoaling of the northern sourced waters during
443   glacials produces a mid-depth well-ventilated water mass that feeds into the Caribbean through its
444   deepest sill (~1900 m, Johns et al., 2002). Thus the deep Caribbean is filled with less corrosive waters
445   during glacials than interglacials improving the preservation of carbonate during glacials in a similar
446   pattern to a Pacific styled dissolution cycle albeit in response to Atlantic circulation changes. During
447   interglacials, the Northern sourced waters are mixed with corrosive southern sourced waters (Antarctic
448   Intermediate Waters and upper circumpolar deep waters) leading to less well-preserved sediments.

449   **4.2 Causes of offset between $\delta^{11}B$ –derived and ice core CO_2.**

450   The $\delta^{11}B$-derived CO_2 record from both of our study sites is in very good agreement with the ice core
451   record, with an average offset for combined both cores of 4.6 ±49 (2σ) ppm and corresponding RMSE
452   of 24.7 ppm. The CO_2 offset calculated with Mg/Ca-SST corrected for pH is shown in Figure S8 for
453   comparison and the average is -4.8 ±42 (2σ) ppm, showing a reduced offset of 9 ppm compared to
454   treatment with no pH correction on SST (a difference of -11 ±14 (2σ) and -8 ±12 (2σ) ppm at ODP
455   site 871 and 999, respectively). This difference is due to the pH correction lowering the SST estimates
456   on average without greatly changing the temporal structure of pH and CO_2 offsets.
457   In both treatments, the RMSE is smaller than the average CO_2 uncertainty of ±48 ppm (2σ, 95%
458   confidence) for each datapoint. However, the minor CO_2 offsets observed in both records do not appear
459   to be random and tend to fall during the first half of each glacial cycle (Figure S2). In order to have the
460   highest confidence in CO_2 reconstructions using $\delta^{11}B$, this pattern warrants further investigation (see
461   below). We only discuss the CO_2 records calculated without a pH correction on SST.

462   *4.2.1 Comparison between morphotypes of G. ruber*

463   If as others suggested (e.g. Wang et al., 2000; Steinke et al., 2005; Numberger et al., 2009) *G. ruber sl*
464   and *G. ruber ss* occupied different depth habitats, then inadvertent sampling of the cryptic *G. ruber sl*
465   morphotype might conceivably produce the biases we observe between $\delta^{11}B$-derived CO_2 and
466   atmospheric CO_2 from the ice cores. However, while our Mg/Ca-derived temperatures for *G. ruber sl*
467   and *G. ruber ss* display variable offsets, they are within uncertainty (Figure 2) and our $\delta^{18}O$ and $\delta^{13}C$
468   data for the two morphotypes at ODP 871 show a good agreement with no consistent differences (Figure
469   S4). Thus, while the water column profile of $\delta^{18}O$ and $\delta^{13}C$ can be affected by factors other than
470   temperature, salinity and biological productivity (e.g, carbonate ion effect, Spero et al., 1997), overall,
471   our data suggest that the two morphotypes we analysed shared similar depth habitat preferences.

472   Henehan et al. (2013) found that *G. ruber ss* and *sl* record similar $\delta^{11}B$ in core-top sediments, and
473   through necessity, used mixed morphotypes in their culture study. The $\delta^{11}B$-derived pH and CO_2 for *G.*
474   *ruber sl* examined here are consistently higher and lower, than *G. ruber ss* by around 0.05 pH units and
475   15 ppm CO_2, respectively (Figure 3). This is contrary to expectation if *G. ruber sl* lived in deeper more
476   acidic waters as suggested by other studies (Wang et al., 2000; Steinke et al., 2005), but consistent with
477   some data sets that show that the habitat of *G. ruber ss* and *sl* can vary by location (Numberger et al.,
478   2009). We acknowledge that the scarcity of *G. ruber sl* in our samples means that our data set for this
479   morphotype is too small to draw firm conclusions and this warrants further investigation at other study
480   sites. Nonetheless, the closeness of the morphotypes in terms of $\delta^{11}B$ and depth habitat throughout our
481   record implies any inadvertent sampling of *G. ruber sl* in the *G. ruber ss* fraction in this study and
482   location would not significantly bias our reconstructions.

483   *4.2.2   Change in upwelling and CO_2 disequilibrium.*

484   ODP sites 871 and 999 are both located today in stratified oligotrophic environments with a deep
485   modern thermocline (base of the thermocline is at ~ 200 and 400 m at ODP 871 and 999, respectively;
486   Olsen et al., 2016). It should be noted, however, that both sites are situated relatively close to regions
487   displaying ΔpCO_2 >40 ppm (Figure 1). However, if local upwelling occurred over the study interval,
488   or if these areas of upwelled water expanded, we would expect these periods to be characterised by
489   relatively low SST, high surface $\delta^{18}O$, and low surface $\delta^{13}C$ due to an increased influence of deep colder
490   and more remineralised waters. The identified anomalous intervals in residual CO_2 at ODP 871 (e.g at
491   ~210, ~290 ky, Figure 5) show no particular anomaly in planktonic C and O isotopes (Figure S4) or in
492   SST (Figure 2, Figure S9), ruling out significant variations in upwelling at that site. Equally, no SST
493   anomaly was identified at ODP 999 to be coincident with the intervals of high residual CO_2 (Figure S9).
494   This suggests the CO_2 anomalies revealed in Figure 5 are not the result of enhanced local disequilibrium
495   via sub-surface water mixing.

496   *4.2.3   Partial dissolution.*

497   The CO_2 derived from *G. ruber* $\delta^{11}B$ at ODP 999 and 871 appears to show, at first order at least, positive
498   CO_2 offset during periods of high fragmentation (~100, ~210, ~400ky, red filled circles in Figure 5,
499   defined by the upper 25% quantile of fragments) following a "Pacific style" dissolution cycle (better
500   preservation and lower fragmentation during glacial periods). Periods of high fragmentation at ODP
501   site 999 and 871 both (incidentally) correspond to a positive CO_2 offset 75% of the time, and 25% to a
502   negative CO_2 offset, (note that values close to 0 were omitted in this calculation). We also note that
503   almost all CO_2 offsets uncertainty (2σ) overlap with the 0 line, hence the percentage of CO_2 offset that
504   are above or below the 0 line should be interpreted with caution.
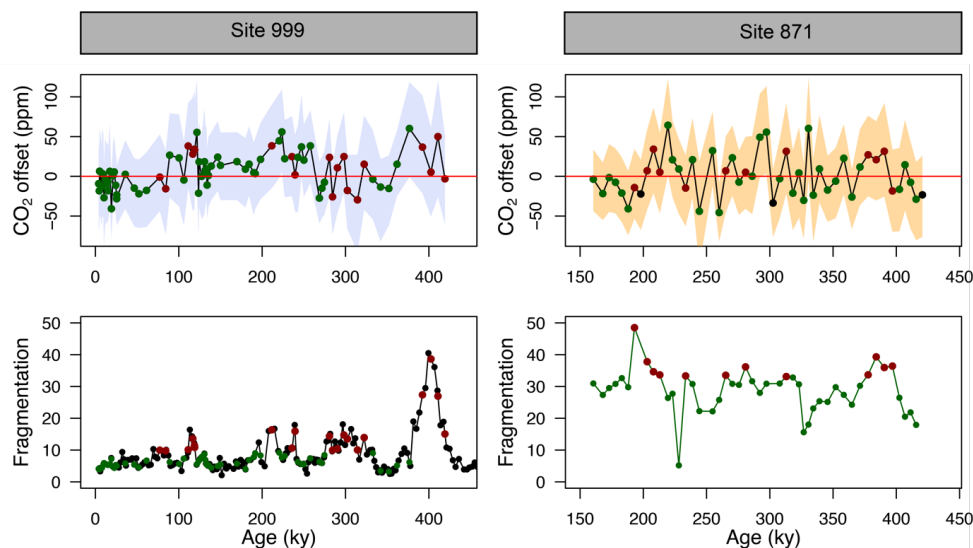
505
506
507   Figure 5. Top panels: CO_2 offset (defined as offset = $CO_{2\_\delta11B\text{-derived}}$ − CO_{2_ice}) for ODP Sites 999 (this study and
508   Chalk et al., 2017) and 871. See text for error bars calculations. Bottom panels: fragmentation index at Site 999
509   (Schmidt et al., 2006) and 871 (this study). Red dots in the lower panels are the fragments above the upper quartile
510   (and corresponding CO_2 in the upper panel, red dots). Green dots represent periods of low fragments below the
511   upper quartile (and corresponding CO_2 in the upper panel, green dots).
512

513   In detail however, a cross-plot of fragment counts and CO_2 offset (Supplementary Figure S10) fitted
514   with a linear regression shows no significant correlation for both core site 999 (r^2=0.07, p=0.02) and
515   871 (r^2=0.01, p=0.62). Although it should be noted that this simple linear regression presupposes a
516   linear relationship between the variables and does not account for the significant uncertainty in both
517   CO_2 offset and fragmentation index. In particular, the CO_2 offset carries the uncertainty from the
518   interpolated ice core CO_2 (see methods). Fragment counts at ODP 999 also come with the additional
519   uncertainty related to the interpolation of the record of Schmidt et al. (2006), whereas fragments counts
520   and δ^{11}B-derived CO_2 at 871 are measured on the same samples. A cross-correlation function also shows
521   no correlation between CO_2 offset and fragmentation (Figure S11).

522   While it seems unlikely the small offsets observed are fully explained by partial dissolution, the positive
523   CO_2 offsets observed during some periods of high fragmentation index (Figure 5), are in line with the
524   trend observed in *T. sacculifer* during our dissolution experiments that showed a decreased δ^{11}B (that
525   translates to higher CO_2) with progressive dissolution (supplementary Figure S6). However our
526   dissolution tests, are consistent with field studies (e.g. Seki et al., 2010), and suggest that *G. ruber* δ^{11}B
527   is relatively robust to dissolution (see section 3.4 above). The pattern observed here for *T. sacculifer*
528   has been documented in other studies where lower δ^{11}B is observed for core-top samples from deeper
529   ocean sites bathed by waters with low calcite saturation state (Hönisch and Hemming, 2004, Seki et al.,
530   2010). Tests of *T. sacculifer* can contain a significant proportion of gametogenic calcite (ranging 30 to
531   75% of the weight of pregametogenic calcite , Bé, 1980; Caron et al 1990) which forms at the end of
532   the life cycle in deeper lower pH cold waters. It has been suggested that δ^{11}B is lower in gametogenic
533   calcite than in the primary test (Ni et al., 2007) reflecting the digestion and expulsion of symbionts (Bé
534   et al., 1983) before gametogenesis, driving a relative acidification of the micro-environment (no CO_2
535   uptake by photosynthesis) around the foraminifera (Zeebe et al. 2003; Hönisch et al,. 2003; Henehan et
536   al. 2016), and movement to deeper more acidic waters during that life-stage. It has also been shown that
537   this gametogenic calcite is more resistant to dissolution (Hemleben et al., 1989; Wycech et al., 2018)
538   resulting in partial dissolution acting preferentially on ontogenic calcite driving δ^{11}B in the residual test
539   to lower isotopic composition.

540   While the decrease in δ^{11}B in dissolved test of *T. sacculifer* is well explained by the lighter isotopic
541   composition of gametogenic calcite, *G. ruber* tests do not contain such gametogenic calcite (Caron et
542   al., 1990). Hence, if the observed occasional decrease in δ^{11}B (low pH, high CO_2) was caused by partial
543   dissolution, it needs to be explained by other processes. It should also be considered that the dissolution
544   experiments performed here could be of longer duration (e.g. Caron et al., 1990; Sadekov et al., 2010)
545   and be more quantitative (e.g. with alkalinity of leaching acid, trace element data and foraminifera
546   weight data to evaluate the degree of dissolution over time). Furthermore, alternative measures and
547   proxies of dissolution may yield more quantitative constraints (e.g. benthic B/Ca as an indicator of
548   bottom water carbonate ion concentration) on the importance of dissolution in generating our observed
549   CO_2 offsets.

550   Some studies have shown that laboratory dissolved specimens of *T. sacculifer* (Sadekov et al., 2010)
551   and naturally dissolved specimens of *G. ruber* (Iwasaki et al., 2019) undergo targeted partial preferential
552   dissolution of the shell. However, variations in intra-shell δ^{11}B are currently unknown due to limitations
553   in laser ablation techniques that impede a direct evaluation of δ^{11}B heterogeneity in foraminifera
554   chambers. Future studies are needed to constrain the δ^{11}B spatial distribution in foraminiferal shells
555   caused by potential variations in δ^{11}B from dissolution, ontogeny (e.g. Meilland et al., 2021) and/or
556   vital effects (e.g. change in photosymbiotic activity throughout the life cycle, Lombard et al., 2009,
557   Henehan et al., 2013, Takagi et al., 2019).

558   In the absence of these constraints, and given the limitations of our dissolution experiments, we
559   conclude that partial dissolution is unlikely to be a significant driver of the δ^{11}B-CO_2 records we present
560   here. Even though it was thought to be a species susceptible to dissolution (Berger, 1970), we confirm
561   that the δ^{11}B of *G. ruber* appears more resistant to dissolution-driven modification than *T. sacculifer*.

562   *4.2.4.   Effect of dissolution on Mg/Ca and calculated CO_2.*

563 The direction of change of Mg/Ca with partial dissolution is towards lower ratios in partially dissolved
564 foraminifera (e.g. Brown and Elderfield, 1996; Dekens et al., 2002; Fehrenbacher and Martin, 2014). If
565 the Mg/Ca is impacted during periods of high fragmentation, the lower ratio would result in lower
566 temperatures leading to lower calculated CO_2 values (equation 7). This effect is opposite to the
567 occasional positive deviation of CO_2 observed during intervals of high fragmentation at ODP Site 999.
568 While the weak correlation between fragmentation and CO_2 precludes a firm interpretation of
569 dissolution effect, we conclude that the effect of partial dissolution on Mg/Ca ratio and resulting CO_2
570 (if any) is negligeable and not responsible for the CO_2 offsets observed during intervals of high
571 fragmentation.
572

573   *4.2.5.   Change in the second carbonate parameter, alkalinity.*

574 Past changes in TA are poorly constrained, although some constraints are starting to emerge for the late
575 Quaternary (e.g. Cartapanis et al., 2018). However, since pH is directly determined by $\delta^{11}B$, pH defines
576 the ratio of alkalinity to DIC (see supplementary information S12). Hence, at any given pH, any change
577 in alkalinity must be counteracted by a change in DIC, which has the opposing effect on CO_2. This is
578 demonstrated by the tight relation between pH and CO_2 highlighted by our data (Figure 4). The largest
579 residual CO_2 is ~50 ppm at ODP 999. To produce an effective alkalinity-driven change in CO_2 of this
580 magnitude at a given pH requires an alkalinity reduction of about ~300 to 500 μmol/mol (supplementary
581 Figure S13). This is far larger than any expected change over a glacial cycle (Cartapanis et al., 2018,
582 Hönisch et al., 2009). We therefore rule out varying TA as the cause of the minor CO_2 offsets observed
583 (Figure 5).

584   *4.2.6   Improving the $\delta^{11}B$ -pH G. ruber calibration*

585 A further potential cause for the minor offsets observed between $\delta^{11}B$-derived and ice core CO_2 could
586 be a small inaccuracy in the calibration between $\delta^{11}B$ of foraminifera and borate for *G. ruber* (Henehan
587 et al., 2013). Having the ice core data to compare with $\delta^{11}B$-derived CO_2 offers an opportunity to explore
588 the effect of altering the input variables of the pH-CO_2 calculation to see if doing so improves the fit to
589 ice-core values. Note that such an exercise is for illustrative purposes only because we seek to retain
590 the independence offered by the $\delta^{11}B$-calibrated data in the context of CO_2 forcing (section 4.3).
591 Nonetheless, in future work we suggest this calibration can be applied in tandem to the empirical
592 relationship of Henehan et al. (2013). The published (Henehan et al., 2013) and obtained optimised
593 calibration (Figure S14) are:

594 $$\delta^{11}B_{borate} = \frac{\delta^{11}B_{foram}-8.87(\pm1.52)}{0.60(\pm0.09)} \quad \text{(Henehan et al., 2013)}$$

595 $$\delta^{11}B_{borate} = \frac{\delta^{11}B_{foram}-6.46}{0.72} \quad \text{(optimised calibration)}$$

596 The newly calculated CO_2 with the updated calibration shows an improved average CO_2 offset (Figure
597 6) of -3.43 ± 41 (2σ) ppm (vs 4.6 ± 49 (2σ) ppm with the calibration of Henehan et al., 2013) and an
598 RMSE of 20.68 ppm (vs. 25 ppm with the published calibration).

599
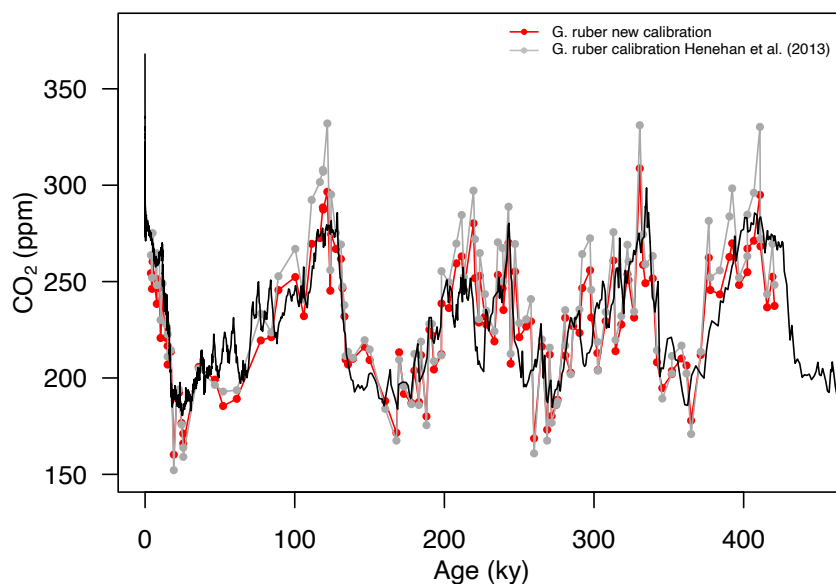
601 Figure 6. Composite δ^{11}B-derived CO_2 from both core sites 999 and 871 using the published $\delta^{11}B_{borate\text{-}foram}$
602 calibration (grey points, Henehan et al., 2013) and the improved calibration (red points). The black line is the
603 Antarctic composite ice core CO_2 record (Bereiter et al., 2015).

604 When analysing the CO_2 offset using the optimised *G. ruber* calibration and the fragmentation index at
605 each core location (same approach as Figure 5), we observe that intervals of high fragments (defined as
606 values above the upper quartile) are no longer preferentially associated with positive CO_2 offset (Figure
607 S15). Intervals of high fragments at site 999 have 50% chance of corresponding CO_2 with positive
608 offsets to the ice core (and 50% with negative offset to the ice core). Intervals of high fragments at site
609 871 have 56% of corresponding CO_2 with a positive offset to the ice core (and 44% with a negative
610 offset to the ice core). This analysis shows that a small change in the borate *G. ruber* δ^{11}B calibration
611 does not cause any visual correlation between CO_2 offset and fragmentation index (Figure S15), and
612 that uncertainty in the $\delta^{11}B_{foram\text{-}borate}$ calibration of Henehan et al. (2013) can – at least partly – explain
613 the minor discrepancies we observe between δ^{11}B-derived and ice core CO_2.

4.3 Relative CO₂ forcing and pH.

615 Our new pH data, added to the existing compilation, show a good agreement with the formalism defined
616 by Hain et al. (2018; Figure 4). It should be noted that CO_2 in this case is provided by the ice core
617 directly and is not estimated from the δ^{11}B-derived pH. As discussed above, because these two proxies
618 are independent of one another, the slope of their relationship may be used to interrogate the
619 mechanisms of CO_2 change. Our data fall between the $CaCO_3$ (yellow plain line) and the DIC (dotted-
620 dashed blue line) end-members suggesting that the CO_2 change observed on glacial-interglacial
621 timescales was driven by a mix of mechanisms rather than to a single cause. This is in line with studies
622 that require a number of mechanisms to explain glacial interglacials CO_2 change (soft tissue pump,
623 carbonate compensation pump and thermal pump, e.g. Brovkin et al., 2007, Kohfeld and Ridgwell,
624 2009, Hain et al., 2010, Chalk et al., 2019, Sigman et al., 2021). We note that this is a preliminary
625 interpretation because of the sensitivity of our finding to pH uncertainty (section 3.5, Figure S7). To
626 overcome this ambiguity in estimating past ΔFCO_2 and to better deconvolve the driving mechanisms of
627 glacial/interglacial CO_2 change, we recommend that future studies collect pH data at higher temporal

628 resolution to examine the change in slope through a glacial cycle and strive to further quantify and
629 reduce uncertainties related to pH determination.

630 The close agreement of the pH and ice core CO_2 data with the theoretical relationships has a number of
631 consequences for the reconstruction of CO_2 change during periods of Earth history beyond the ice core
632 CO_2 and climate records where constrains on $\delta^{11}B_{sw}$ and the second carbonate parameter and
633 temperature are uncertain. The ΔpH formalism still requires an estimation of $\delta^{11}B_{SW}$ and temperature
634 (for the pK_B term, equation 5) however, as discussed in Hain et al. (2018), while absolute reconstruction
635 of pH is significantly influenced by estimates of $\delta^{11}B_{sw}$ and temperature, reconstruction of relative pH
636 change (ΔpH) is inherently much less sensitive to these input variables.

637 Reconstructing ΔF_{CO2} from ΔpH is ideally applicable only on relatively short timescales less than 1
638 Myrs, when $\delta^{11}B_{sw}$ is likely to be constant given the multi-million year residence time of boron in the
639 ocean (Lemarchand et al., 2000, Greenop et al., 2017). Furthermore, to reconstruct ΔF_{CO2} (and thus
640 climate sensitivity to CO_2), the formalism can be applied as long as, in equation 2, ΔpH remains the
641 overwhelming control. This is dependent on the residence time of carbon in the ocean with respect to
642 silicate weathering – approximately one million years (Hain et al., 2018) such that net carbon addition
643 to or removal from the Earth System through volcanic outgassing or silicate weathering is likely to be
644 minor over the million-year timescale. However, during some short events, such as for instance the
645 Palaeocene-Eocene Thermal Maximum, considerable carbon was added to the system in <200 kyr (e.g.
646 Gutjahr et al., 2017) invalidating the formulation described in equation 2 on these intervals. We also
647 emphasize that this formalism is only valid as long as core sites remain in equilibrium with the
648 atmosphere.

649 **4.4 Caveats and future studies.**

650 The aim of this study is to evaluate the capacity of the $\delta^{11}B$-pH proxy in *G. ruber* to accurately
651 reconstruct atmospheric CO_2 in the past. The overall agreement with the high confidence ice core CO_2
652 (e.g. Bereiter et al., 2015) is very promising and gives confidence to $\delta^{11}B$-derived CO_2 reconstructions
653 beyond the ice core record (>800 ky). We have however identified occasional, minor offsets between
654 the two records and explored potential drivers (partial dissolution, $\delta^{11}B$ borate-foram calibration, local
655 air-sea disequilibrium). It is likely that the minor disagreement observed (Figure 5) has a combination
656 of drivers and that a single mechanism is not solely responsible for the CO_2 offsets observed. To confirm
657 these trends, we recommend future work to focus on the following:

658 (1) The improved $\delta^{11}B$ calibration approach should be tested at more core locations. We note that the
659 improved calibration to the ice core records reported here was achieved using data from two sites. While
660 care is taken in the choice of study site to minimize air-sea CO_2 disequilibrium and sediment dissolution,
661 the newly defined improved $\delta^{11}B_{borate-foram}$ calibration should be seen as an exercise that is tailored to the
662 available data in this study, and future high-resolution studies can apply the method used here (section
663 4.4.5) to further test how the *G. ruber* calibration changes if CO_2 offsets occur in a similar fashion (i.e
664 at a particular time in each glacial cycles). We note the importance of high resolution (at least 3 ky)
665 sampling in future studies because most CO_2 offsets observed are short lived.

666 (2) A multiproxy approach is ideally needed. In particular, reliable indicators of temperature and
667 productivity, to assess change in upwelling and foraminifera ecology. We encourage future studies to
668 expand high resolution boron-derived CO_2 record and ancillary data (C and O isotopes, proxy of
669 carbonate preservation and bottom water corrosiveness, biological productivity) to further constrain the
670 capacity of the boron isotope pH/CO_2 proxy to generate reliable CO_2 records. As more recent IODP
671 expeditions include porewater data, constraints on bottom water conditions and degree of corrosiveness
672 at a given site will become available to evaluate the impact on $\delta^{11}B$ signals in foraminifera.

Climate
of the Past
Discussions

673   (3) Efforts should continue to decrease the analytical uncertainty associated with a $\delta^{11}B$ measurement
674   by MC-ICPMS because this still accounts for ~40% of the total uncertainty associated with each $\delta^{11}B$-
675   derived CO_2 estimate.

676   (4) We find little evidence to suggest that partial dissolution of foraminiferal tests (*G. ruber*) is a major
677   driver of uncertainty in $\delta^{11}B$–derived CO_2 estimates but more thorough experiments are desirable
678   because of site-to-site differences in foraminifera taphonomy.
679
680   **5. Conclusion.**

681   We carried out the most thorough test to date of the $\delta^{11}B$–pH (CO_2) proxy by comparing new high-
682   resolution (3 to 6 ky per sample) boron isotope–based pH and CO_2 at two locations with CO_2 from the
683   ice core record. Results suggest that the boron isotope proxy is robust and suited to reconstructing CO_2
684   to a precision of ±48 ppm (2σ, RMSE =25ppm) over this interval, with little or no systematic bias
685   shown by a mean residual of 4.6 ± 49 (2σ) ppm. This provides high confidence to the application of
686   the proxy beyond the reach of the ice core records.

687   Despite the overall good agreement, there are some minor short-lived CO_2 offsets that appear to have
688   some temporal structure and we explored a number of possible drivers. A visual correlation between
689   CO_2 offset and fragmentation index at core site 999 is observed (Figure 5) but is not statistically
690   significant. The effect of partial dissolution on $\delta^{11}B$ in *G. ruber* appears to be negligeable in our record,
691   but the possible heterogeneity of $\delta^{11}B$ within shells as well as variable susceptibly to dissolution of the
692   different parts of the foraminifera, encourages further exploration.

693   An revised $\delta^{11}B$ borate–foram calibration was calculated by minimising the offset between $\delta^{11}B$–
694   derived CO_2 and ice core CO_2 using published calibration (Henehan et al., 2013). While the new
695   calibration improves the fit to the ice core records, we caution against its use to estimate CO_2 given that
696   it is no longer independent of the ice core or the assumptions we make here to calculate CO_2 (i.e. that
697   TA is constant).

698   The formalism established by Hain et al. (2018) is robust, showing that relative CO_2 forcing in the past
699   can be determined from pH change alone, even in the face of significant uncertainty in $\delta^{11}B$ of seawater
700   and without the need to determine a second carbonate parameter. This will not only be of great interest
701   to determine CO_2 forcing in ancient geological times where $\delta^{11}B$ of seawater and a second carbonate
702   parameter are poorly constrained, but the nature of the observed relationship over the last 400 kyr
703   confirms that multiple drivers are likely responsible for glacial-interglacial CO_2 change.

704   **6. Data availability.**
705   All raw data will be provided as supplementary information once the manuscript is accepted.
706
707   **7. Author contribution.**
708   E.d.l.V generated boron isotope and elemental data and wrote the manuscript. E.d.l.V, T.B.C, M.P.H
709   and G.L.F analysed the data. G.L.F, T.B.C, M.P.H and P.A.W contributed to the editing and
710   reviewing of the manuscript. M.W, R.G and D.C generated oxygen and carbon isotope data and
711   fragmentation index data. R.G and D.C were supervised by T.B.C and G.L.F. C.L assisted with
712   foraminifera picking and boron isotope analysis. E.d.l.V, T.B.C and G.L.F designed the research.
713
714   **8. Competing interest.**
715   The authors declare they have no conflict of interest.
716

722
723
724 **10. References.**

725
726 Ahn, J., et al. (2012). "Atmospheric CO2 over the last 1000 years: A high-resolution record
727 from the West Antarctic Ice Sheet (WAIS) Divide ice core." Global Biogeochemical Cycles
728 **26**(2).

729
730 Anagnostou, E., et al. (2020). "Proxy evidence for state-dependence of climate sensitivity in
731 the Eocene greenhouse." Nature communications **11**(1): 1-9.

732
733 Anagnostou, E., et al. (2016). "Changing atmospheric CO2 concentration was the primary
734 driver of early Cenozoic climate." Nature **533**(7603): 380-384.

735
736 Anagnostou, E., et al. (2019). "Calibration of the pH-δ11B and temperature-Mg/Li proxies in
737 the long-lived high-latitude crustose coralline red alga Clathromorphum compactum via
738 controlled laboratory experiments." Geochimica et Cosmochimica Acta **254**: 142-155.

739
740 Anand, P., et al. (2003). "Calibration of Mg/Ca thermometry in planktonic foraminifera from
741 a sediment trap time series." Paleoceanography **18**(2).

742
743 Aurahs, R., et al. (2011). "A revised taxonomic and phylogenetic concept for the planktonic
744 foraminifer species Globigerinoides ruber based on molecular and morphometric evidence."
745 Marine Micropaleontology **79**(1-2): 1-14.

746
747 Barker, S., et al. (2006). "Globally increased pelagic carbonate production during the Mid-
748 Brunhes dissolution interval and the CO2 paradox of MIS 11." Quaternary Science Reviews
749 **25**(23-24): 3278-3293.

750
751 Barker, S., et al. (2003). "A study of cleaning procedures used for foraminiferal Mg/Ca
752 paleothermometry." Geochemistry, Geophysics, Geosystems **4**(9).

753
754 Bé, A. (1980). "Gametogenic calcification in a spinose planktonic foraminifer, Globigerinoides
755 sacculifer (Brady)." Marine Micropaleontology **5**: 283-310.

756
757 Bé, A. W., et al. (1983). "Sequence of morphological and cytoplasmic changes during
758 gametogenesis in the planktonic foraminifer Globigerinoides sacculifer (Brady)."
759 Micropaleontology: 310-325.

760
761 Bereiter, B., et al. (2015). "Revision of the EPICA Dome C CO2 record from 800 to 600 kyr
762 before present." Geophysical Research Letters **42**(2): 542-549.

763
764 Berger, W. H. (1970). "Planktonic foraminifera: selective solution and the lysocline." Marine
765 Geology **8**(2): 111-138.

766
767 Boyle, E. A. (1988). "The role of vertical chemical fractionation in controlling late Quaternary
768 atmospheric carbon dioxide." Journal of Geophysical Research: Oceans **93**(C12): 15701-
769 15714.

770

771　Boyle, E. A. (1988). "Vertical oceanic nutrient fractionation and glacial/interglacial
772　CO2cycles." Nature **331**(6151): 55-56.
773
774　Brovkin, V., et al. (2007). "Lowering of glacial atmospheric CO2 in response to changes in
775　oceanic circulation and marine biogeochemistry." Paleoceanography **22**(4).
776
777　Brown, S. J. and H. Elderfield (1996). "Variations in Mg/Ca and Sr/Ca ratios of planktonic
778　foraminifera caused by postdepositional dissolution: Evidence of shallow Mg-dependent
779　dissolution." Paleoceanography **11**(5): 543-551.
780
781　Caron, D. A., et al. (1990). "Effects of gametogenesis on test structure and dissolution of some
782　spinose planktonic foraminifera and implications for test preservation." Marine
783　Micropaleontology **16**(1-2): 93-116.
784
785　Cartapanis, O., et al. (2018). "Carbon burial in deep-sea sediment and implications for oceanic
786　inventories of carbon and alkalinity over the last glacial cycle." Climate of the Past **14**(11):
787　1819-1850.
788
789　Carter, A., et al. (2017). "Differing oxygen isotopic signals of two Globigerinoides ruber
790　(white) morphotypes in the East China Sea: Implications for paleoenvironmental
791　reconstructions." Marine Micropaleontology **131**: 1-9.
792
793　Chalk, T., et al. (2019). "Dynamic storage of glacial CO2 in the Atlantic Ocean revealed by
794　boron [CO32−] and pH records." Earth and Planetary Science Letters **510**: 1-11.
795
796　Chalk, T. B., et al. (2017). "Causes of ice age intensification across the Mid-Pleistocene
797　Transition." Proceedings of the National Academy of Sciences **114**(50): 13114-13119.
798
799　De La Vega, E., et al. (2020). "Atmospheric CO2 during the Mid-Piacenzian Warm Period and
800　the M2 glaciation." Scientific reports **10**(1): 1-8.
801
802　Dekens, P. S., et al. (2002). "Core top calibration of Mg/Ca in tropical foraminifera: Refining
803　paleotemperature estimation." Geochemistry, Geophysics, Geosystems **3**(4): 1-29.
804
805　Dyez, K. A., et al. (2018). "Early Pleistocene obliquity-scale pCO2 variability at∼ 1.5 million
806　years ago." Paleoceanography and Paleoclimatology **33**(11): 1270-1291.
807
808　Dyez, K. A. and A. C. Ravelo (2013). "Late Pleistocene tropical Pacific temperature sensitivity
809　to radiative greenhouse gas forcing." Geology **41**(1): 23-26.
810
811　Dyez, K. A. and A. C. Ravelo (2014). "Dynamical changes in the tropical Pacific warm pool
812　and zonal SST gradient during the Pleistocene." Geophysical Research Letters **41**(21): 7626-
813　7633.
814
815　Farrell, J. W. and W. L. Prell (1989). "Climatic change and CaCO3 preservation: An 800,000
816　year bathymetric reconstruction from the central equatorial Pacific Ocean." Paleoceanography
817　**4**(4): 447-466.
818

819   Fehrenbacher, J. S. and P. A. Martin (2014). "Exploring the dissolution effect on the intrashell
820   Mg/Ca variability of the planktic foraminifer Globigerinoides ruber." Paleoceanography **29**(9):
821   854-868.

823   Foster, G. (2008). "Seawater pH, pCO2 and [CO2− 3] variations in the Caribbean Sea over the
824   last 130 kyr: A boron isotope and B/Ca study of planktic foraminifera." Earth and Planetary
825   Science Letters **271**(1-4): 254-266.

827   Foster, G., et al. (2010). "Boron and magnesium isotopic composition of seawater."
828   Geochemistry, Geophysics, Geosystems **11**(8).

830   Foster, G. L., et al. (2012). "The evolution of pCO2, ice volume and climate during the middle
831   Miocene." Earth and Planetary Science Letters **341**: 243-254.

833   Foster, G. L., et al. (2013). "Interlaboratory comparison of boron isotope analyses of boric acid,
834   seawater and marine CaCO3 by MC-ICPMS and NTIMS." Chemical Geology **358**: 1-14.

837   Foster, G. L. and J. W. Rae (2016). "Reconstructing ocean pH with boron isotopes in
838   foraminifera." Annual Review of Earth and Planetary Sciences **44**: 207-237.

840   Gray, W. R. and D. Evans (2019). "Nonthermal influences on Mg/Ca in planktonic
841   foraminifera: A review of culture studies and application to the last glacial maximum."
842   Paleoceanography and Paleoclimatology **34**(3): 306-315.

844   Greenop, R., et al. (2017). "A record of Neogene seawater δ11B reconstructed from paired
845   δ11B analyses on benthic and planktic foraminifera." Climate of the Past **13**(2): 149-170.

847   Guillermic, M., et al. (2022). "Atmospheric CO 2 estimates for the Miocene to Pleistocene
848   based on foraminiferal δ 11 B at Ocean Drilling Program Sites 806 and 807 in the Western
849   Equatorial Pacific." Climate of the Past **18**(2): 183-207.

851   Gutjahr, M., et al. (2017). "Very large release of mostly volcanic carbon during the Palaeocene–
852   Eocene Thermal Maximum." Nature **548**(7669): 573-577.

854   Hain, M., et al. (2018). "Robust constraints on past CO2 climate forcing from the boron isotope
855   proxy." Paleoceanography and Paleoclimatology **33**(10): 1099-1115.

857   Hain, M. P., et al. (2010). "Carbon dioxide effects of Antarctic stratification, North Atlantic
858   Intermediate Water formation, and subantarctic nutrient drawdown during the last ice age:
859   Diagnosis and synthesis in a geochemical box model." Global Biogeochemical Cycles **24**(4).

861   Hansen, J., et al. (2008). "Target atmospheric CO2: Where should humanity aim?" arXiv
862   preprint arXiv:0804.1126.

864   Harper, D., et al. (2020). "The magnitude of surface ocean acidification and carbon release
865   during Eocene Thermal Maximum 2 (ETM-2) and the Paleocene-Eocene Thermal Maximum
866   (PETM)." Paleoceanography and Paleoclimatology **35**(2): e2019PA003699.

868   Hemleben, C., et al. (1989). Modern Planktonic Foraminifera, Springer-Verlag.

869
870 Henehan, M. J., et al. (2016). "A new boron isotope-pH calibration for Orbulina universa, with
871 implications for understanding and accounting for 'vital effects'." Earth and Planetary Science
872 Letters **454**: 282-292.

873
874 Henehan, M. J., et al. (2015). "Evaluating the utility of B/C a ratios in planktic foraminifera as
875 a proxy for the carbonate system: A case study of G lobigerinoides ruber." Geochemistry,
876 Geophysics, Geosystems **16**(4): 1052-1069.

877
878 Henehan, M. J., et al. (2013). "Calibration of the boron isotope proxy in the planktonic
879 foraminifera Globigerinoides ruber for use in palaeo-CO2 reconstruction." Earth and Planetary
880 Science Letters **364**: 111-122.

881
882 Henehan, M. J., et al. (2019). "Rapid ocean acidification and protracted Earth system recovery
883 followed the end-Cretaceous Chicxulub impact." Proceedings of the National Academy of
884 Sciences **116**(45): 22500-22504.

885
886 Hönisch, B., et al. (2003). "The influence of symbiont photosynthesis on the boron isotopic
887 composition of foraminifera shells." Marine Micropaleontology **49**(1-2): 87-96.

888
889 Hönisch, B. and N. G. Hemming (2004). "Ground-truthing the boron isotope-paleo-pH proxy
890 in planktonic foraminifera shells: Partial dissolution and shell size effects." Paleoceanography
891 **19**(4).

892
893 Hönisch, B. and N. G. Hemming (2005). "Surface ocean pH response to variations in pCO2
894 through two full glacial cycles." Earth and Planetary Science Letters **236**(1-2): 305-314.

895
896 Hönisch, B., et al. (2009). "Atmospheric carbon dioxide concentration across the mid-
897 Pleistocene transition." Science **324**(5934): 1551-1554.

898
899 Howard, W. R. and W. L. Prell (1994). "Late Quaternary CaCO3 production and preservation
900 in the Southern Ocean: Implications for oceanic and atmospheric carbon cycling."
901 Paleoceanography **9**(3): 453-482.

902
903 Iwasaki, S., et al. (2019). "Micro-CT Scanning of Tests of Three Planktic Foraminiferal Species
904 to Clarify DissolutionProcess and Progress." Geochemistry, Geophysics, Geosystems **20**(12):
905 6051-6065.

906
907 John, S. G. and J. F. Adkins (2010). "Analysis of dissolved iron isotopes in seawater." Marine
908 chemistry **119**(1-4): 65-76.

909
910 Johns, W. E., et al. (2002). "On the Atlantic inflow to the Caribbean Sea." Deep sea research
911 part I: Oceanographic research papers **49**(2): 211-243.

912
913 Klochko, K., et al. (2006). "Experimental measurement of boron isotope fractionation in
914 seawater." Earth and Planetary Science Letters **248**(1-2): 276-285.

915
916 Kohfeld, K. E. and A. Ridgwell (2009). "Glacial-interglacial variability in atmospheric CO2."
917 Surface ocean-lower atmosphere processes **187**: 251-286.
918

919   Lee, K., et al. (2010). "The universal ratio of boron to chlorinity for the North Pacific and North
920   Atlantic oceans." Geochimica et Cosmochimica Acta **74**(6): 1801-1811.

921

922   Lemarchand, D., et al. (2002). "Boron isotope systematics in large rivers: implications for the
923   marine boron budget and paleo-pH reconstruction over the Cenozoic." Chemical Geology
924   **190**(1-4): 123-140.

925

926   Lisiecki, L. E. and M. E. Raymo (2005). "A Plio-Pleistocene stack of 57 globally distributed
927   benthic δ 18 O records." Paleoceanography **20**: 1-17.

928

929   Lombard1, F., et al. (2009). "Temperature effect on respiration and photosynthesis of the
930   symbiont-bearing planktonic foraminifera Globigerinoides ruber, Orbulina universa, and
931   Globigerinella siphonifera." Limnology and Oceanography **54**(1): 210-218.

932

933   Lueker, T. J., et al. (2000). "Ocean pCO2 calculated from dissolved inorganic carbon,
934   alkalinity, and equations for K1 and K2: validation based on laboratory measurements of CO2
935   in gas and seawater at equilibrium." Marine chemistry **70**(1-3): 105-119.

936

937   Lüthi, D., et al. (2008). "High-resolution carbon dioxide concentration record 650,000–800,000
938   years before present." Nature **453**(7193): 379-382.

939

940   Martínez-Botí, M., et al. (2015). "Plio-Pleistocene climate sensitivity evaluated using high-
941   resolution CO 2 records." Nature **518**(7537): 49.

942

943   Meilland, J., et al. (2021). "Population dynamics and reproduction strategies of planktonic
944   foraminifera in the open ocean." Biogeosciences **18**(20): 5789-5809.

945

946   Ni, Y., et al. (2007). "A core top assessment of proxies for the ocean carbonate system in
947   surface-dwelling foraminifers." Paleoceanography **22**(3).

948

949   Numberger, L., et al. (2009). "Habitats, abundance patterns and isotopic signals of
950   morphotypes of the planktonic foraminifer Globigerinoides ruber (d'Orbigny) in the eastern
951   Mediterranean Sea since the Marine Isotopic Stage 12." Marine Micropaleontology **73**(1-2):
952   90-104.

953

954   Olsen, A., et al. (2016). "The Global Ocean Data Analysis Project version 2 (GLODAPv2)–an
955   internally consistent data product for the world ocean." Earth System Science Data **8**(2): 297-
956   323.

957

958   Olsen, A., et al. (2004). "Sea–air flux of CO2 in the Caribbean Sea estimated using in situ and
959   remote sensing data." Remote Sensing of Environment **89**(3): 309-325.

960

961   Oppo, D. and S. Lehman (1993). "Mid-depth circulation of the subpolar North Atlantic during
962   the last glacial maximum." Science **259**(5098): 1148-1152.

963

964   Paillard, D., et al. (1996). "Macintosh program performs time-series analysis." Eos,
965   Transactions American Geophysical Union **77**(39): 379-379.

966

967   Penman, D. E., et al. (2014). "Rapid and sustained surface ocean acidification during the
968   Paleocene-Eocene Thermal Maximum." Paleoceanography **29**(5): 357-369.

969
970   Petit, J.-R., et al. (1999). "Climate and atmospheric history of the past 420,000 years from the
971   Vostok ice core, Antarctica." Nature **399**(6735): 429-436.
972
973   Premoli-Silva, I. (1993). Shipboard Scientific Party, 1993a Site 871. Proc. ODP, Init. Repts.
974
975   Rae, J. W., et al. (2011). "Boron isotopes and B/Ca in benthic foraminifera: Proxies for the
976   deep ocean carbonate system." Earth and Planetary Science Letters **302**(3-4): 403-413.
977
978   Raitzsch, M., et al. (2018). "Boron isotope-based seasonal paleo-pH reconstruction for the
979   Southeast Atlantic–A multispecies approach using habitat preference of planktonic
980   foraminifera." Earth and Planetary Science Letters **487**: 138-150.
981
982   Rohling, E., et al. (2013). "Making sense of palaeoclimate sensitivity (vol 491, pg 683, 2012)."
983   Nature **494**(7435): 130-130.
984
985   Rohling, E. J., et al. (2018). "Comparing climate sensitivity, past and present." Annual Review
986   of Marine Science **10**: 261-288.
987
988
989   Sadekov, A. Y., et al. (2010). "Effects of seafloor and laboratory dissolution on the Mg/Ca
990   composition of Globigerinoides sacculifer and Orbulina universa tests—A laser ablation
991   ICPMS microanalysis perspective." Earth and Planetary Science Letters **292**(3-4): 312-324.
992
993   Sanyal, A., et al. (1995). "Evidence for a higher pH in the glacial ocean from boron isotopes in
994   foraminifera." Nature **373**(6511): 234-236.
995
996   Schlitzer, R. (2022). "Ocean data view."
997
998   Schmidt, M. W., et al. (2006). "Western Caribbean sea surface temperatures during the late
999   Quaternary." Geochemistry, Geophysics, Geosystems **7**(2).
1000
1001 Seki, O., et al. (2010). "Alkenone and boron-based Pliocene pCO2 records." Earth and
1002 Planetary Science Letters **292**(1-2): 201-211.
1003
1004 Sexton, P. F. and S. Barker (2012). "Onset of 'Pacific-style'deep-sea sedimentary carbonate
1005 cycles at the mid-Pleistocene transition." Earth and Planetary Science Letters **321**: 81-94.
1006
1007 Siegenthaler, U., et al. (2005). "Stable carbon cycle climate relationship during the Late
1008 Pleistocene." Science **310**(5752): 1313-1317.
1009
1010 Sigman, D. M., et al. (2021). "The Southern Ocean during the ice ages: A review of the
1011 Antarctic surface isolation hypothesis, with comparison to the North Pacific." Quaternary
1012 Science Reviews **254**: 106732.
1013
1014 Sigman, D. M., et al. (1998). "The calcite lysocline as a constraint on glacial/interglacial low-
1015 latitude production changes." Global Biogeochemical Cycles **12**(3): 409-427.
1016
1017 Spero, H. J., et al. (1997). "Effect of seawater carbonate concentration on foraminiferal carbon
1018 and oxygen isotopes." Nature **390**(6659): 497-500.

1019
1020   Steinke, S., et al. (2005). "Mg/Ca ratios of two Globigerinoides ruber (white) morphotypes:
1021   Implications for reconstructing past tropical/subtropical surface water conditions."
1022   Geochemistry, Geophysics, Geosystems **6**(11).
1023
1024   Takagi, H., et al. (2019). "Characterizing photosymbiosis in modern planktonic foraminifera."
1025   Biogeosciences **16**(17): 3377-3396.
1026
1027   Takahashi, T., et al. (2009). "Climatological mean and decadal change in surface ocean pCO_2,
1028   and net sea–air CO_2 flux over the global oceans." Deep Sea Research Part II: Topical Studies
1029   in Oceanography **56**(8-10): 554-577.
1030
1031   Toggweiler, J. (1999). "Variation of atmospheric CO_2 by ventilation of the ocean's deepest
1032   water." Paleoceanography **14**(5): 571-588.
1033
1034   Wang, L. (2000). "Isotopic signals in two morphotypes of Globigerinoides ruber (white) from
1035   the South China Sea: implications for monsoon climate change during the last glacial cycle."
1036   Palaeogeography, Palaeoclimatology, Palaeoecology **161**(3-4): 381-394.
1037
1038   Wycech, J. B., et al. (2018). "Combined effects of gametogenic calcification and dissolution
1039   on $\delta18O$ measurements of the planktic foraminifer Trilobatus sacculifer." Geochemistry,
1040   Geophysics, Geosystems **19**(11): 4487-4501.
1041
1042   York, D., et al. (2004). "Unified equations for the slope, intercept, and standard errors of the
1043   best straight line." American journal of physics **72**(3): 367-375.
1044
1045   Zeebe, R. E. and D. Wolf-Gladrow (2001). CO_2 in seawater: equilibrium, kinetics, isotopes,
1046   Gulf Professional Publishing.
1047
1048   Zeebe, R. E., et al. (2003). "Vital effects in foraminifera do not compromise the use of $\delta11B$
1049   as a paleo-pH indicator: Evidence from modeling." Paleoceanography **18**(2).
1050

1051

1052